



Dual-sided centripetal microgrooved poly (D,L-lactide-co-caprolactone) disk encased in immune-regulating hydrogels for enhanced bone regeneration

You Wu^{a,b,1}, Xiaokun Yue^{c,1} , Ying Zhang^{a,b}, Ning Yu^d, Chengyan Ge^e, Rui Liu^{a,b}, Zhongying Duan^{a,b}, Lilong Gao^f, Xinlong Zang^b, Xin Sun^{g,**}, Deteng Zhang^{a,b,*} 

^a China Uruguay Bio-Nano Pharmaceutical Joint Laboratory, Institute of Neuroregeneration and Neurorehabilitation, Qingdao University, 308 Ningxia Road, Qingdao, 266071, Shandong, China

^b Qingdao Medical College, Qingdao University, Qingdao, 266071, China

^c Shanghai Key Laboratory of Orthopaedic Implants, Department of Orthopaedic Surgery, Shanghai Ninth People's Hospital, Shanghai Jiao Tong University School of Medicine, No. 639 Zhizaoju Road, Shanghai, 200011, China

^d Department of Anesthesiology, Affiliated Hospital of Qingdao University, No. 16 Jiangsu Road, Qingdao, 266000, Shandong, China

^e Department of Neurosurgery, Affiliated Hospital of Qingdao University, No. 16 Jiangsu Road, Qingdao, 266000, Shandong, China

^f School of Materials Science and Engineering, Qingdao University, Qingdao, 266071, China

^g Department of Orthopaedics, Shanghai Sixth People's Hospital Affiliated to Shanghai Jiao Tong University School of Medicine, No. 600 Yishan Road, Shanghai, 200233, China

ARTICLE INFO

Keywords:

Centripetal microgrooves
Immune regulation
Hydrogels
Prussian blue nanoparticles
Bone regeneration

ABSTRACT

Well-designed artificial scaffolds are urgently needed due to the limited self-repair capacity of bone, which hampers effective regeneration in critical defects. Optimal scaffolds must provide physical guidance to recruit cells and immune regulation to improve the regenerative microenvironment. This study presents a novel scaffold composed of dual-sided centripetal microgrooved poly(D,L-lactide-co-caprolactone) (PLCL) film combined with a dynamic hydrogel containing prednisolone (PLS)-loaded Prussian blue nanoparticles (PB@PLS). The microgrooves on the surface of the PLCL film were imprinted using a micropatterned polydimethylsiloxane (PDMS) template. Following aminolysis, the PLCL film was covalently grafted with the EM-7 peptide via glutaraldehyde. Functional group analysis, surface morphology and hydrophilicity were evaluated using X-ray photoelectron spectroscopy (XPS), scanning electron microscopy (SEM), and an optical contact angle measuring instrument, respectively. Bone regeneration-related cells (e.g., bone marrow mesenchymal stem cells, macrophages, Schwann cells, and endothelial cells) cultured on PLCL films tended to align along the stripes and migrate from the periphery toward the center region *in vitro*. Subsequently, the PLCL film was encapsulated in an immune-regulating hydrogel synthesized from thiol-modified gelatin and Cu²⁺ in the presence of PB@PLS nanoparticles, which demonstrated excellent antioxidant properties. This scaffold significantly accelerated critical-sized bone regeneration, as evidenced by an increase in the volume of newly formed bone and histological images *in vivo*. This innovative approach holds substantial promise for clinical applications in bone regeneration and broader tissue repair.

1. Introduction

Critical-sized bone defect is highly prevalent due to trauma, tumors, congenital malformations, and acquired developmental abnormalities

[1]. Bone provides structural support and maintains the overall organization of the human body [2]. Mature bone's hierarchical, anisotropic structure, which comprised of dense cortical and spongy cancellous bone, is critical to its mechanical function. The Haversian system,

* Corresponding author. China Uruguay Bio-Nano Pharmaceutical Joint Laboratory, Institute of Neuroregeneration and Neurorehabilitation, Qingdao University, 308 Ningxia Road, Qingdao, 266071, Shandong, China.

** Corresponding author.

E-mail addresses: doctor_sunxin@163.com (X. Sun), zhangbio137@qdu.edu.cn (D. Zhang).

¹ Co-first author.

<https://doi.org/10.1016/j.mtbio.2024.101436>

Received 14 October 2024; Received in revised form 22 December 2024; Accepted 28 December 2024

Available online 3 January 2025

2590-0064/© 2024 Published by Elsevier Ltd. This is an open access article under the CC BY-NC-ND license (<http://creativecommons.org/licenses/by-nc-nd/4.0/>).

containing nerves and blood vessels, ensures nutrient delivery and neural communication. Cancellous bone's trabeculae house hematopoietic and mesenchymal stem cells, supporting bone regeneration and hematopoiesis [3]. Bone's self-repair capacity is significant but limited. Defects exceeding this capacity can trigger chronic inflammation, potentially resulting in prolonged or incomplete healing [4]. Autografts are considered the gold standard for bone regeneration in clinical practice [5]. Nevertheless, they present several challenges, such as the requirement for a secondary surgical procedure, limited donor availability, potential mismatches in donor tissue volume, and delays in surgical scheduling [6]. Tissue engineering offers a promising approach to repairing osteoporotic bone defects. Advances in biocompatible scaffolds with sufficient strength, appropriate degradation rates, and enhanced osteogenic activity are central to this field [6,7].

Rapid recruitment of various cells and stem cells to the injury site can accelerate the regeneration of the central area, significantly influencing the overall repair rate of the damaged region [8–10]. Enhancing the migration of autologous stem cells can effectively reduce the immune rejection and infection risks associated with the transplantation of foreign cells. Numerous studies have demonstrated that cell-substrate interactions can modulate cellular behavior through diverse mechanisms. The contact interfaces include groove-ridge patterns, oriented electrospun fibers, nanoparticle-enhanced surfaces, and microporous surfaces [11–15]. Biochemical cues, such as cytokines introduced through chemical grafting, play a pivotal role in cellular behavior. Previous studies have demonstrated that oriented microgroove structures of a specific size can induce the directed migration of Schwann cells (SCs) while concurrently promoting the polarization of macrophages towards the M2 phenotype [11,12,16]. Therefore, we investigated the application of topographic structures in critical-sized bone repair.

This study is inspired by the structure of a spider's web. The intricate webs spun by spiders serve as effective tools for capturing their prey. Spider silk contains mucus secreted by the spiders, which enables them to maneuver across the web's surface and effectively stabilize their captured prey. Whether the spider captures its prey in the center or along the edges of the web, the radial structure allows the spider to reach the prey in the shortest distance and with the fastest speed [17,18]. This concept inspires us to fabricate a "spider web" liked structure using a radial centripetal microgroove architecture to capture cells within the bone defect area. This design aims to promote the migration of healthy cells from the periphery toward the center of the injury, thereby facilitating bone repair. In this study, we utilized a biodegradable polymer, poly(D,L-lactide-co-caprolactone) (PLCL), to fabricate a dual-sided centripetal microgrooved PLCL (MG-PLCL) film. This film effectively captures endogenous repair cells in the vicinity of the injury site and guides their migration towards the defect center. Furthermore, an optimal "web" for cell capture must not only provide essential physical support and directional guidance for cell migration but also deliver biochemical cues and assist in modulating the hostile regenerative microenvironment [4]. Zheng et al. reported that bone marrow mesenchymal stem cells (BMSCs)-targeting EM-7 peptides (pep) are affinity peptides that specifically bind to and capture BMSCs. Furthermore, as the density of the pep increases, there is a notable enhancement in the number, adhesion area, and adhesive capabilities of cells on biological materials [19]. In our study, we modified the surface of MG-PLCL with pep using a chemical grafting method to enhance its adhesive properties, creating an excellent cell-catching "web".

In the initial stage of a bone defect, ischemia and hypoxia resulting from vascular injury and acute inflammation create a detrimental microenvironment for bone regeneration. This adverse condition disrupts the balance between oxidative and antioxidative pathways, leading to the accumulation of reactive oxygen species (ROS) and the polarization into a pro-inflammatory M1 phenotype [20,21]. Reducing the accumulation of ROS and the secretion of pro-inflammatory factors can promote the transformation of M1 phenotype macrophages into the

anti-inflammatory M2 phenotype [22]. This shift aids in the secretion of anti-inflammatory factors and mediators that can recruit osteogenesis related cells. By modulating the microenvironment in this manner, conditions can be optimized to facilitate bone regeneration [23]. Prednisolone (PLS) is a glucocorticoid with potent anti-inflammatory properties, commonly employed in clinical practice. However, its direct high-dose administration is frequently linked to adverse inflammatory responses, which can restrict its therapeutic application. This limitation is further exacerbated by the compound's non-targeted action, poor water solubility, and short half-life [24–26]. Notably, the utilization of nanodelivery systems can significantly expand the application of PLS. These systems enhance the drug's targeting capabilities, improve its solubility, and prolong its half-life, thereby optimizing therapeutic effectiveness while minimizing adverse effects. Prussian blue nanoparticles (PB) serve as promising drug delivery vehicles due to their unique chemical composition and hollow structure, which enable them to mimic multiple enzyme effects and facilitate efficient drug delivery [27]. Additionally, these nanoparticles possess photothermal properties and exhibit excellent biocompatibility [28,29]. Consequently, utilizing the biological features of PB nanoparticles for the transport of PLS can effectively regulate bone regeneration by optimizing the oxidative and inflammatory microenvironment.

Gelatin is renowned for its excellent biocompatibility and biodegradability, which promote cell adhesion and facilitate its widespread applications in bone tissue engineering [30]. Yang et al. employed sulfhydryl gelatin (Gel-SH) at the tendon-to-bone interface, leveraging its ability to form reversible covalent bonds with copper ions (Cu^{2+}). This approach has been shown to enhance bone regeneration by regulating osteoblast differentiation and promoting angiogenesis [31]. In this study, we developed a novel artificial scaffold featuring a pep modified dual-sided centripetal microgrooved surface (MG-PLCL/pep), combined with dynamic hydrogels capable of delivering prednisolone-loaded PB nanoparticles (PB@PLS) for the repair of critical-sized bone defects (Fig. 1). We thoroughly characterized the fundamental physicochemical properties of the scaffolds, focusing on topography, size, antioxidant capacity, anti-inflammatory effects, and biocompatibility. Additionally, we assessed the guidance of bone regeneration-related cells *in vitro*. The scaffolds were subsequently implanted into bone defects in rats, and we conducted systematic micro-CT and histological analyses of the newly formed bone.

2. Materials and methods

2.1. Materials

PLCL (L-lactide and ϵ -caprolactone with a molar ratio of 75: 25, Mw 35 kDa) were customized from Jinan Daigang Biotech Co., Ltd., China. Freeze-dried Gel-SH were kindly obtained from Guoqing Pan's group in Jiangsu University, China. Hollow mesoporous prussian blue nanoparticles were purchased from Nanjing Jike Biotechnology Co., Ltd. The prepolymer and cross-linking agent to generate polydimethylsiloxane were purchased from Dow, USA. Anhydrous ethanol, 1,4-dioxane, 1, 6-hexanediamine, tert-butanol, isopropyl alcohol, Copper (II) sulfate pentahydrate and glutaraldehyde (25 %) were purchased from Sino-pharm Chemical Reagent Co., China. Polyformaldehyde fixative (4 %) was purchased from Lanjiek Technology Co., Ltd. Ninhydrin hydrate (98 %) was obtained from Macklin Biochemical Co., Ltd. EM-7 peptides were customized from GL Biochem Ltd., China. Milli-Q water was used for all the experiments (Millipore, USA).

2.2. Preparation and characterization of dual-sided centripetal MG-PLCL films

2.2.1. Preparation of dual-sided centripetal MG-PLCL films

0.3 g of PLCL was dissolved in 3 mL of 1,4-dioxane to create a homogeneous solution, which was then degassed under vacuum and

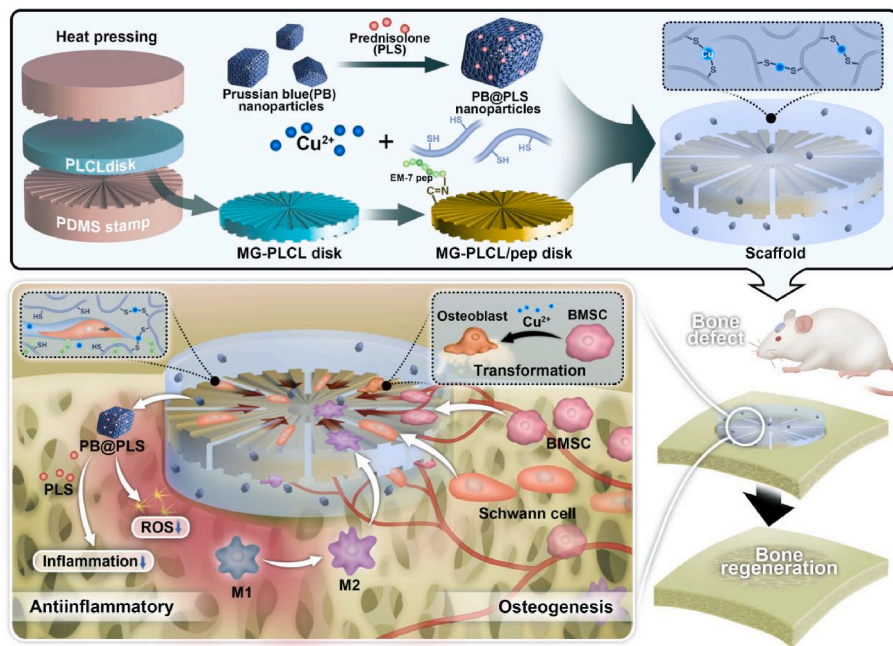


Fig. 1. Schematic illustration of the synthesis and preparation of the dual-sided centripetal microgrooved immune-regulating scaffold for enhanced bone regeneration.

poured into a custom polytetrafluoroethylene (PTFE) mold, allowing a PLCL film to form as the solvent evaporated. Dual-sided centripetal microgrooves were imprinted on the film using a two-step replicating template method. Polydimethylsiloxane (PDMS) stamps with complementary microstructures were first fabricated from microgrooved silicon master plates. The microgrooved PDMS stamps were pressed onto both sides of the PLCL film at 190 °C, ensuring precise alignment while the film was in a viscous state. In contrast, the flat PLCL (F-PLCL) film was prepared using flat PDMS in a viscous flow state. Subsequently, the films were immersed in a 10 % (v/v) solution of 1,6-hexamethylenediamine in isopropyl alcohol for 10 min to introduce amine groups, followed by thorough washing with plenty of water. The films were then soaked in a 2 % (v/v) glutaraldehyde solution for 3 h, rinsed, and treated with pep solution for another 3 h to promote polypeptide grafting. Finally, a 0.5 mm diameter punch was used to create a hole at the center of the circular pattern on the film, followed by eight radial cuts directed towards the center, resulting in a three-dimensional (3D) centripetal topographic guiding scaffold with upper and lower connecting structures.

2.2.2. Characterization of dual-sided centripetal MG-PLCL films

The surface morphology of the PLCL films and PDMS stamps were observed by scanning electron microscope (SEM, Zeiss Sigma 500, Germany) after gold spraying. The hydrophilicity of the films was measured by optical contact angle measuring instrument (Krüss DSA30S, Germany). The ninhydrin assay was used to quantify the graft density of dual-sided amino groups on PLCL films. Pep grafted on PLCL films was characterized by X-ray photoelectron spectroscopy (XPS, Shimadzu Axis Supra+, Japan). The degradation experiments were performed by soaking PLCL films in phosphate buffered saline (PBS) and incubating them on a shaking bed at 37 °C. The films were removed at a fixed time (1, 3, 5, 7, 14, 21, 28 days), then dried and weighed. The initial weight of the films was recorded as W_0 , and the weight of the films at different time points was recorded as W_t . The degradation rate was calculated based on the formula: degradation rate (%) = $(W_0 - W_t) / W_0 \times 100$ %.

2.3. Preparation and characterization of hydrogel containing PB@PLS

2.3.1. Preparation of PB@PLS and hydrogel

Equal volumes of 1 mg/mL PB were mixed with 5 mg/mL PLS and stirred under vacuum for 30 min. The mixture was then centrifuged at 10,000 g for 15 min. Following this, the freeze-dried Gel-SH was resuspended in the PB@PLS solution and dissolved at 50 °C to obtain 10 % Gel-SH hydrogel prepolymer. This solution was transferred into a cylindrical PTFE mold with a diameter of 0.5 cm. The PLCL film was then immersed in the hydrogel solution, which was mixed with a 0.05 M copper sulfate solution to form a cohesive glue [31]. The volume ratio of hydrogel prepolymer and copper sulfate solution was 20: 6.

2.3.2. Characterization of PB and PB@PLS

The morphology of mesoporous PB and PB@PLS were observed by transmission electron microscope (TEM, Hitachi HT7700, Japan). The average size of nanoparticles was calculated by quantitative analysis of TEM images. The size and charge of the nanoparticles were measured by using the particle size and Zeta potential analyzer (Brookhaven, OMNI, USA). The release of PLS from PB@PLS was also measured according to the standard curve analyzed by ultraviolet spectrophotometry (Shimadzu, UV-2700, Japan). The antioxidant capacity of the particles was characterized by DPPH free radical scavenging ability detection kit (Solarbio, China) *in vitro*.

2.3.3. Characterization of hydrogel

The content of sulfhydryl in Gel-SH was determined by Total Sulfhydryl Assay Kit with DTNB (Solarbio, China). The morphology was observed by SEM after breaking in liquid nitrogen, and the pore sizes were quantified by SEM images. The rheological behavior was evaluated using a dynamic visco-elastic spectrometer (Rheometer, TA DHR3, USA). Each sample was tested between 40 mm aluminate parallel plates with a gap of 3 mm maintained at 37 °C using 200 μ L hydrogel. The frequency for strain sweep measurements was set at 1 Hz, with a strain range of 0.1 %–1000 %. For oscillation frequency measurements, a strain of 1 % was maintained while varying the frequency from 0.1 rad/s to 100 rad/s. The compression properties of the scaffolds were evaluated by universal material testing machine (Instron 5300, USA), with a speed

set at 0.1 N/min. The compression modulus was calculated for deformations ranging from 5 % to 25 %. Each set of experiments included 6 parallel samples. Additionally, the swelling rate of the hydrogel was determined by soaking the freeze-dried hydrogel in PBS and measuring its weight at various time intervals (1, 2, 3, 4, 5, 6, 12, and 24 h). Before weighing, the samples were taken out, and excess surface water was absorbed using filter paper. The initial weight of the freeze-dried hydrogel was W_a , the weight at different times was W_x , and the swelling rate (%) = $(W_x - W_a) / W_a \times 100$ %.

2.4. Cell evaluation

2.4.1. BMSCs and bone marrow-derived macrophages isolation and culture

Sprague-Dawley rats (3 weeks old) and C57BL/6 mice (8 weeks old) were obtained from Jinan Pengyue Experimental Animal Breeding Co., LTD. (Shandong, China). According to the previous method, the animals were first euthanized and soaked in 75 % alcohol for sterilization [32]. Both legs were removed, and the soft tissue was carefully stripped in a safety cabinet. Cuts were made at the epiphyses of both the femur and tibia. BMSCs were collected from rats via the α -MEM (Procell, Wuhan, China) flushing out the bone marrow of the rats while bone marrow-derived macrophages (BMDMs) were obtained from mice using DMEM (Solarbio, China) treatment.

2.4.2. Antioxidant capacity of PB and PB@PLS in vitro

5×10^3 cells were seeded in the 48-well plate and cultured for 12 h. Then the culture medium was exchanged into DMEM (Control), 750 μ M H_2O_2 in DMEM, 20 μ g/mL PB and 750 μ M H_2O_2 in DMEM, 20 μ g/mL PB@PLS and 750 μ M H_2O_2 in DMEM. Intracellular ROS level was detected by Dihydroethidium (DHE, Solarbio, China) after 24 h. In addition, cell counting kit-8 (CCK-8, Gibco, USA) was used to detect cell survival at 1, 3, and 5 days.

2.4.3. Cell viability assay

3×10^3 BMSCs were cultured on various films fixed at the bottom of a 96-well plate. The cell viability was assessed using the CCK-8 by measuring absorbance at 450 nm with a microplate reader (Molecular Devices SpectraMax ABS, USA) after 1, 3, and 5 days. To evaluate biocompatibility, Schwann cells and human umbilical endothelial cells (HUVECs) were also cultured on the films using the same procedure.

A hydrogel embedded with PB@PLS was prepared following established protocols [33]. Cells were cultured with the extract for 1, 3, and 5 days, and their proliferation was evaluated using the CCK-8 assay. First, the hydrogel was soaked in PBS for 24 h to eliminate excess sulfate ions. It was then immersed in α -MEM supplemented with 20 mg/mL fetal bovine serum and incubated at 37 °C for an additional 24 h. Subsequently, 3×10^3 per well BMSCs were seeded into a 96-well plate and cultured with the extracts.

2.4.4. Cell morphological characterization

Immunofluorescence staining was performed to characterize the morphology of BMSCs on various PLCL films, including F-PLCL, MG-PLCL, and MG-PLCL/pep. 3×10^4 BMSCs, BMDMs and RAW264.7 were seeded and cultured per well for 3 days and 7 days in a 48-well plate, after which they were fixed with 4 % paraformaldehyde (PFA) for 15 min. Following fixation, the cells were washed with PBS, permeabilized with 0.1 % Triton X-100, and blocked with 5 % bovine serum albumin. F-actin was stained with Alexa Fluor 488 Phalloidin (1:1000; Abcam, UK), and the macrophage markers CCR7 (Proteintech, China) and CD206 (Proteintech, China) were incubated for 2 h. Additionally, cell nuclei were stained with DAPI (Thermo Fisher Scientific, USA). The cell length-to-width ratio and orientation angles relative to the grooves were analyzed using ImageJ software, based on images captured by a fluorescent confocal microscope (Nikon Ti2-E, Japan).

The BMSCs spheroids were fabricated by seeding 5×10^3 cells per well (80 μ L) in a sharp-bottom 96-well plate which pretreated 5 %

pluronic (Sigma, USA) for 12 h. Next, the cell spheroids were transferred on MG-PLCL/pep films and cultured for 24 h, and stained with Calcein AM (Yeasen, China) for fluorescent detection.

BMSCs, SCs, BMDMs, and HUVECs were cultured on PLCL films for 3 days, then fixed in 4 % PFA for 2 h and rinsed with PBS. The samples underwent gradient dehydration used a mixture of tert-butanol and ethanol at concentrations of 5 %, 15 %, 30 %, 50 %, 70 %, and 100 %, with each step lasting 10 min. Finally, the samples were freeze-dried for SEM analysis. Images were analyzed using Image J software to measure the orientation angles of the cytoskeleton, which reflects cell orientation. The cytoskeletal orientation angle was defined as the angle between the longitudinal axis of the cytoskeleton and the axis of the centripetal microgrooves [34].

2.4.5. Expression of osteogenic, angiogenic and neurogenic genes

Real-time quantitative fluorescent PCR (qRT-PCR) was employed to analyze the expression of genes including *ALP*, *Col-1*, *Runx2*, *BSP*, *VEcad*, *PDGF β* , *CD31*, *VEGF α* , *HIF1*, and *Ang1*. BMSCs were differentiated and cultured in osteogenic conditions for 10 days. After culturing HUVECs on the PLCL films for 3 days, total RNA was extracted using the SteadyPure RNA Extraction Kit (Accurate Biology, China). The RNA was quantified with a NanoDrop (Thermo Fisher Scientific, USA) and concentration was normalized. Reverse transcription was conducted using the Evo M-MLV RT Premix for qPCR (Accurate Biology, China) to synthesize complementary DNA (cDNA). qRT-PCR was performed using SYBR Green detection reagent (SYBR Green Premix Pro Taq HS qPCR Kit, Accurate Biology, China), with GAPDH served as the internal control. The primers used were listed in Table S1.

A co-culture system was employed to investigate the expression of ALP, where BMSCs were cultured in the lower chamber and scaffolds were placed in the upper chamber for 7 and 14 days respectively.

2.5. Hemocompatibility assay

5 mL of fresh blood were collected into an anticoagulant tube, centrifuged at 1500 rpm to isolate the red blood cells (RBCs) and washed three times with PBS. The RBCs were then resuspended to create a 2 % (v/v) suspension and co-incubated with the various groups at 37 °C for 12 h. Following incubation, the supernatant was collected, and absorbance at 545 nm was measured. Triton X-100 and PBS served as positive and negative controls in the co-culture with the RBC suspension, respectively.

For the blood coagulation assay, 100 μ L of fresh blood was added to the scaffold. The clotting time was recorded from the moment calcium chloride solution was added. Following complete coagulation, deionized water was added to resuspend the clot, and the absorbance of the supernatant was measured at 545 nm.

2.6. Animal study

All related procedures in this study were approved by the Animal Care and Use Committee of Qingdao University and were carried out in accordance with the guidelines of the National Institutes of Health Guide for Care and Use of Laboratory Animals (No. GB14925-2010). Sprague-Dawley rats (average weight ~250 g) were anesthetized, and a longitudinal incision was made in the skin above the skull. A 5 mm diameter

Table 1
Different compositions scaffolds of animal study groups.

Group	F-PLCL/pep	MG-PLCL/pep	PB@PLS	Hydrogel
Control	–	–	–	–
A	–	–	–	✓
B	✓	–	–	✓
C	–	✓	–	✓
D	–	✓	✓	✓

defect was created bilaterally along the sagittal suture using a circular serrated drill bit. The defect area was then filled with different scaffolds (Table 1), while the control group received no filling. 8 weeks post-surgery, the rats were euthanized, and the skulls were removed and fixed in 4 % PFA for subsequent assessment [35]. The bone volume fraction (BV/TV) and bone mineral density (BMD) was calculated based on the 3D images of micro-CT (PerkinElmer Quantum GX2, Japan). The newly formed bone tissue was observed by Hematoxylin and eosin (H&E) staining and Masson staining.

3. Results and discussion

3.1. Characterization of dual-sided centripetal MG-PLCL/pep film

Critical-sized bone defects can lead to persistent pain, elevated complication rates, and a markedly diminished quality of life. Artificial scaffolds possess physical guidance cues that regulate cell phenotype,

cytoskeleton arrangement, migration and differentiation, along with chemical properties that can reduce ROS. These factors play a crucial role in the immune microenvironment, which significantly impacts bone tissue regeneration. Despite the development of various tissue engineering stents for treating severe bone defects, their therapeutic effects remain unsatisfactory. Moreover, there has not yet been a report on the preparation of an effective topography-guided regulation approach that simultaneously modulates multiple cell scaffolds in conjunction with biochemical signals. In this study, we investigated a dual-sided centripetal MG-PLCL/pep film combined with a dynamic hydrogel made from Gel-SH and Cu^{2+} , loaded with PB@PLS (Fig. 2a). This innovative scaffold effectively regulates cellular adhesion and migration while exhibiting remarkable antioxidant properties. Furthermore, it can significantly enhance bone repair in a rat model, as evidenced by an increase in newly formed bone volume and supportive histological imagery. With its unique topographical cues and inflammation regulation capabilities, this novel scaffold holds substantial promise for clinical

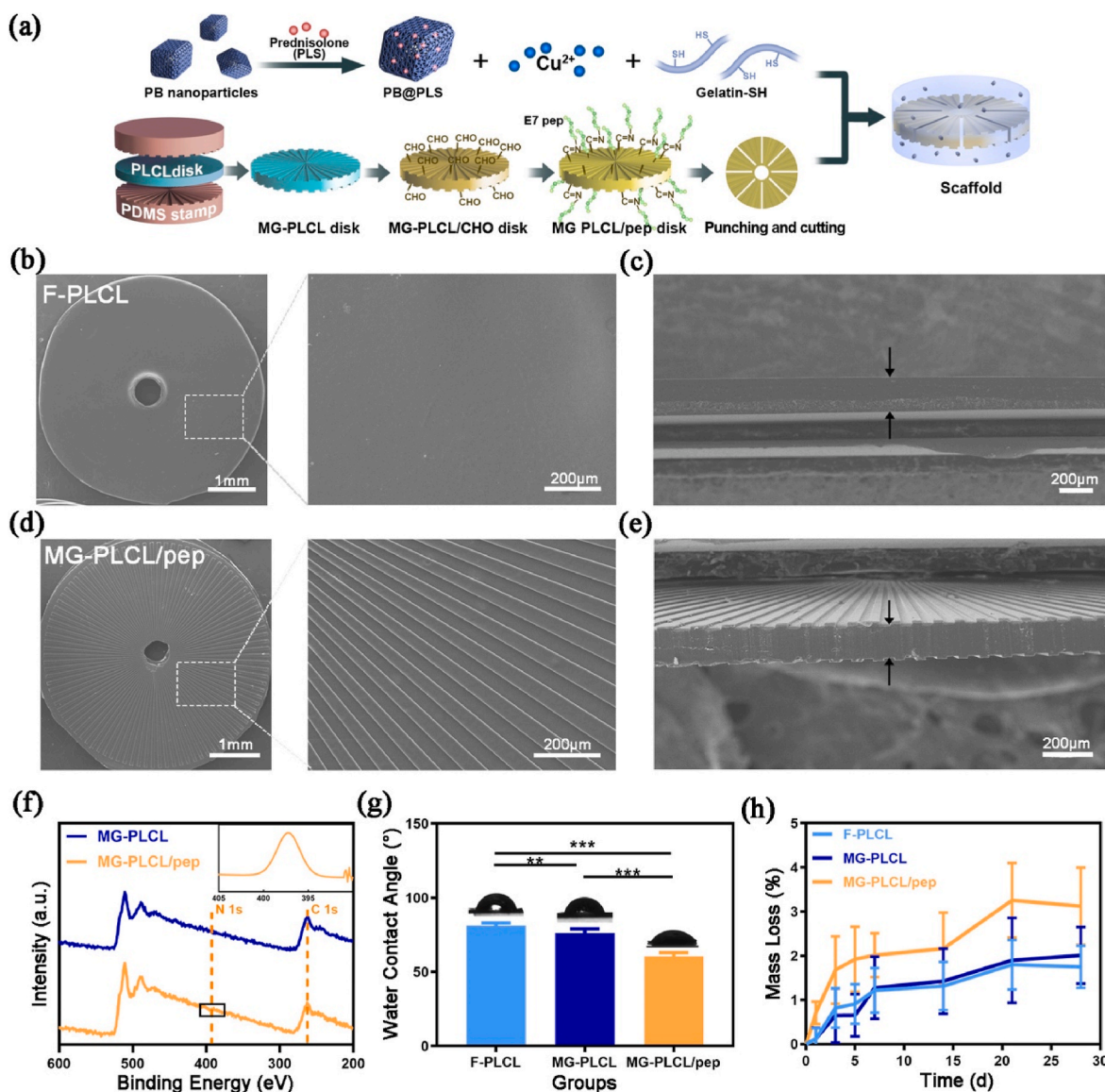


Fig. 2. Characterization of dual-sided centripetal MG-PLCL/pep film. (a) Schematic illustration of the fabrication of MG-PLCL/pep. (b) SEM images of F-PLCL film. The dextral image is a magnified view. (c) SEM images of the cross section of F-PLCL film. The black arrows indicate the cross section. (d) SEM images of MG-PLCL/pep film. The dextral image is magnified view. (e) SEM images of the cross section of MG-PLCL/pep film. The black arrows indicate the cross section. (f) XPS analysis showing the distribution patterns of H, C, N and O contents on various surfaces. High-resolution XPS spectra of N 1s elements of pep on MG-PLCL/pep film. (g) Water contact angle on various films. (h) Degradation behavior of various films in PBS. All data are presented as mean \pm standard deviation (SD). * $p < 0.05$, ** $p < 0.01$, and *** $p < 0.001$.

applications in bone regeneration and the repair of various tissues.

First, a PDMS stamp featuring a centripetal microgroove structure was fabricated from an original silicon wafer mold [12]. SEM images revealed that the width of the microgrooves progressively increased from the center towards the edge, with both the groove and ridge widths at the edge measuring 80 μm , and a microgroove depth of 10 μm (Figs. S1a and b). Notably, MG-PLCL film was successfully replicated on the surface using the PDMS stamp, in contrast to F-PLCL film (Fig. 2b, S1c). The surface of the MG-PLCL/pep film exhibited a well-ordered arrangement of centripetal microgrooves (Fig. 2d). The images demonstrated that the grooves and ridges became wider as they approached the edge, with the width at the edge also measuring 80 μm . Importantly, the chemical modification process did not compromise the micro-structure of the MG-PLCL surface, and the morphology of the microgrooves was unspoiled. In comparison to the cross-section of F-PLCL film, both the upper and lower surfaces of the MG-PLCL film were symmetrically modified with a regular shapes structure, maintaining a depth of 10 μm and a thickness of approximately 150 μm (Fig. 2c, e, Figs. S1d and e). Our fabrication method only requires the application of pressure in a viscous flow state, without being influenced by external environmental factors such as humidity. This approach exhibits more straightforward, controllable, and reproducible. Most importantly, the micro-structure is more stable and remains unaffected by the fabrication process [1,36].

To graft pep onto the MG-PLCL film using glutaraldehyde, amido was first introduced through amolysis. The amino density was measured to be approximately 0.7 $\mu\text{mol}/\text{cm}^2$ through the ninhydrin method [37]. The XPS results exhibited similar C 1s signals at 262.7 eV for both groups; however, a significant enhancement in the N 1s signal at 397.2 eV was observed in the MG-PLCL/pep films (Fig. 2f) [38]. This result confirmed that the peptide was successfully modified.

Surface hydrophilicity is crucial for initial cell interaction, serving as an indicator of cell-material compatibility. Hydrophilic surfaces promote cell adhesion [2]. Water contact angles were 81.1° for the F-PLCL film and 76.2° for the MG-PLCL film (Fig. 2g, Fig. S1 f). Water droplets displayed isotropic distribution on the MG-PLCL film. The multi-directional microgrooves enhanced capillary action, facilitating water droplet spreading. Peptide decoration reduced the contact angle to 60.6°, indicating increased hydrophilicity. This finding was consistent with the results of previous studies [19].

In order to investigate the degradation performance, the quality loss of various films in PBS was measured. There was no significant difference among F-PLCL (1.75 % \pm 0.48) and MG-PLCL (2.01 % \pm 0.64) and MG-PLCL/pep (3.12 % \pm 0.87) groups after 28 days (Fig. 2h). Repairing critical-sized bone defects is a prolonged and complex regenerative process. Suitable biodegradable biomaterials provide mechanical support for tissue regeneration and guide cell infiltration, while their controlled degradation prevents complications and eliminates the need for secondary surgery [2,3]. Overall, we successfully prepared micro-grooved PLCL films with pep modifications, exhibiting hydrophilic surface and regular morphology.

3.2. Characterization of PB@PLS, hydrogels and scaffolds

3.2.1. Characterization of PB@PLS

After tissue damage, a significant amount of ROS is generated. PB nanoparticles have the capability to effectively eliminate these ROS. PLS is effective in reducing inflammation and enhancing the healing process of injured tissue. PB and PB@PLS were characterized by TEM (Fig. 3a and b). As shown in Fig. 3a, the original PB nanoparticles exhibit a hollow cube frame structure. However, after mixing with PLS and stirring under vacuum, the mesoporous pores of PB nanoparticles were filled with it. Although the value of hydrodynamic diameters and polydispersity indices (PDI) of PB (198.0 \pm 4.1 nm, 0.17) and PB@PLS (198.2 \pm 3.7 nm, 0.16) were similar (Fig. 3c, Fig. S2), the Zeta potential was changed from -16.8 ± 1.3 mV to -23.5 ± 1.1 mV (Fig. 3d). Since

PLS carries a negative charge, it is logical that it was successfully loaded.

Bone regeneration is a prolonged repair process characterized by acute inflammation that can last over a week following an injury [23]. The half-life of PLS in the human body is only 4 h, making its slow release advantageous for reducing inflammatory response and enhancing therapeutic efficacy. In our study, we utilized hollow PB nanoparticles as the carrier for PLS, and we evaluated the *in vitro* release profile of PB@PLS. As shown in Fig. 3e, PB@PLS demonstrated sustained and controlled release behavior, with cumulative release reaching approximately 98.9 % after 7 days of incubation.

3.2.2. Antioxidant properties of the PB@PLS

Previous studies have confirmed that PB nanoparticles can effectively remove overproduction of ROS such as hydrogen peroxide (H_2O_2), hydroxyl radical ($\cdot\text{OH}$), and superoxide anion ($\text{O}_2^{\cdot-}$) at the site of injury [39]. DPPH, a single electron free radical, is commonly used to quantitatively assess antioxidant capacity. Our study *in vitro* demonstrated that high concentrations of PB and PB@PLS (1 mg/mL) exhibited enhanced free radical scavenging ability (Fig. 3f). Consequently, we applied the antioxidant PB@PLS at this concentration in subsequent experiments. Notably, the incorporation of PLS significantly improved the free radical clearance rate and bolstered antioxidant capacity across both high and low concentration groups. We hypothesized that the addition of PLS increases the negative charge of PB nanoparticles, facilitating electron loss and enhancing their oxidation potential.

3.2.3. Characterization of hydrogel

The sulfhydryl groups in gelatin could react reversibly with copper ions, resulting in the formation of a dynamic hydrogel (Figs. S3a, b, c) [38]. Firstly, the content of sulfhydryl groups in Gel-SH was quantitatively detected. The standard curve of sulfhydryl concentration/absorbance was drawn by DTNB method to calculate, and the concentration of sulfhydryl in the 10 % w/v hydrogels prepolymer was 3.48 $\mu\text{mol}/\text{L}$ (Fig. S3d). SEM images revealed that micropores are in interconnected condition, evenly distributed, which can be used as a bionic extracellular matrix (ECM) suitable for cell growth (Fig. 3g), and the pore size of hydrogels is about 31.8 ± 5.0 μm (Fig. 3h). As reported, stem cells cultured on a gelatin scaffold with a 30 μm aperture are more likely to differentiate towards osteogenesis [40,41]. In this study, the metal-based dynamic hydrogels could exert regulatory effects on osteogenesis in BMSCs while promoting substance exchange. We assessed the stability and mechanical properties of the hydrogels by evaluating their gel kinetics before and after the introduction of PB@PLS. Frequency scanning was conducted to investigate the changes in storage modulus (G') and loss modulus (G'') with varying strain frequency (Fig. 3j and k). Throughout the entire frequency range, G' consistently surpassed G'' , indicating the formation of stable hydrogels. In comparison to the blank hydrogels, the frequency sweep resulted for hydrogels incorporating PB@PLS (hydrogel/PB@PLS) exhibited minimal variation, suggesting that the addition of nanoparticles did not adversely affect the properties of the hydrogels. Subsequently, the variations in G' and G'' with increasing strain amplitude were evaluated (Fig. 3m and n). As illustrated, G' remained stable within the linear viscoelastic region and then sharply decreased with the continuous increase in strain amplitude, demonstrating a pronounced Payne effect. Notably, under the same strain conditions, the incorporation of PB@PLS significantly enhanced G' while only slightly increasing G'' . This suggested that PB@PLS may augment the cross-linking density of the hydrogel because of the barrier effect of space physics [42]. Furthermore, we evaluated the compression properties of the hydrogels (Fig. S4 a). The stress-strain curves for both groups were nearly identical (Fig. 3i), indicating no significant difference in fracture strength (Fig. S4 b). Additionally, the compression modulus between Hydrogel and Hydrogel/PB@PLS showed no statistical significance (Fig. 3l). These findings suggested that the inclusion of PB@PLS nanoparticles may disrupt the originally stable hydrogels network; although there might be

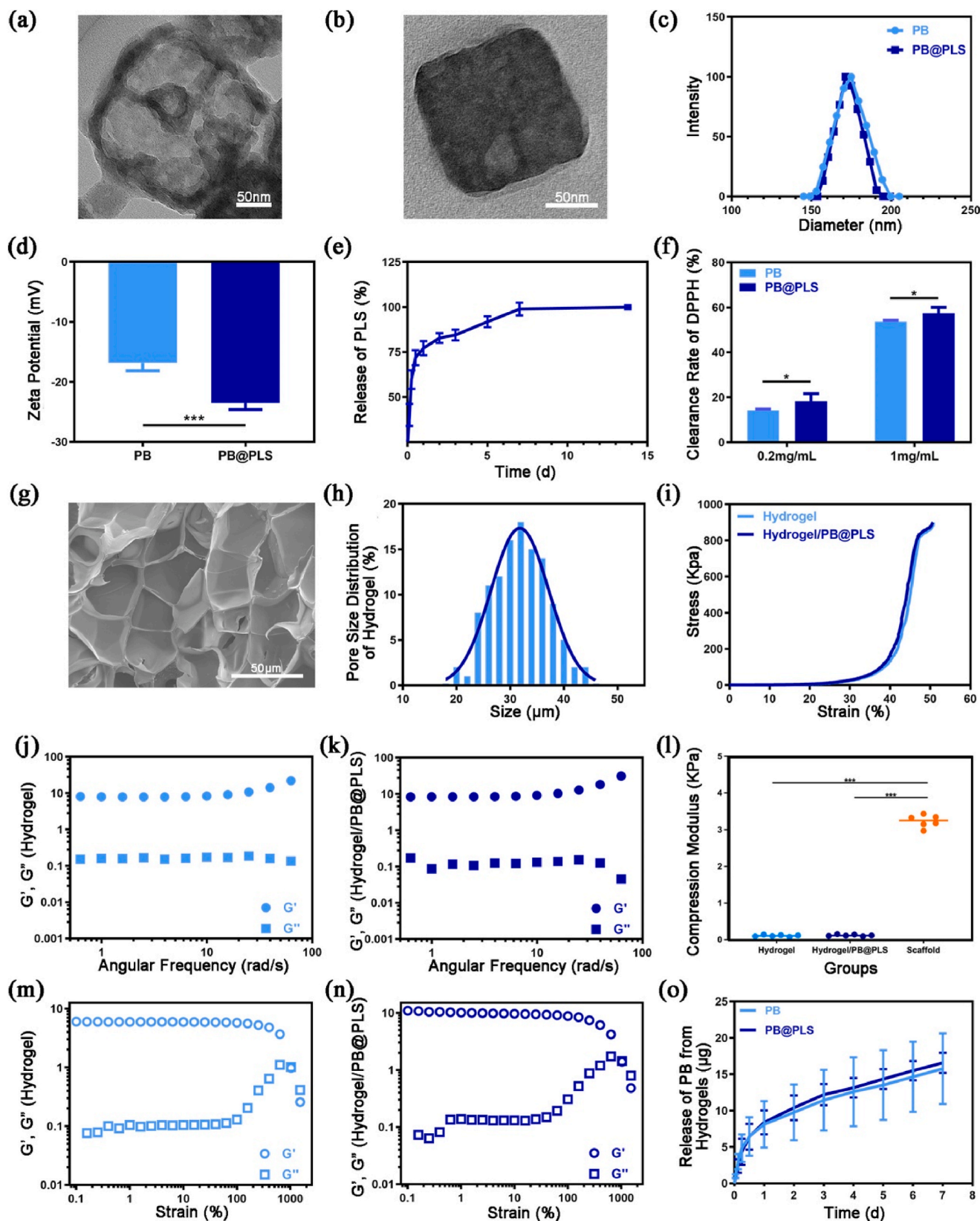


Fig. 3. Characterization of PB@PLS, hydrogels and scaffolds. (a) TEM image of PB nanoparticle. (b) TEM image of PB@PLS nanoparticle. (c) Size distribution of PB and PB@PLS nanoparticles. (d) Zeta potential of PB and PB@PLS nanoparticles. (e) PLS release from PB nanoparticle. (f) The clearance effect of different concentration of PB and PB@PLS nanoparticles on DPPH. (g) SEM image of freeze-dried hydrogel. (h) Pore size distribution calculated by SEM images. (i) Representative compression stress-strain curves (j, k) Frequency sweep measurements of hydrogel and hydrogel/PB@PLS. (l) Compressive modulus of Hydrogel, Hydrogel/PB@PLS and Scaffold. (m to n) Strain sweep measurements of hydrogel and hydrogel/PB@PLS. (o) PB and PB@PLS release curves of hydrogel in PBS. All data are presented as mean \pm SD. * $p < 0.05$, ** $p < 0.01$, and *** $p < 0.001$.

an increase in crosslinking density, it remains below the threshold necessary to affect mechanical properties. Additionally, the supplement of MG-PLCL/pep significantly enhanced the compressive modulus of the hydrogel encapsulating MG-PLCL/pep and PB@PLS (Scaffold). The PLCL film exhibited elasticity and malleability, and did not fracture under stress. Instead, it became flattened and thinner even when subjected to the instrument's maximum load (200 N). Currently, dynamic hydrogels always demonstrate mechanical properties inferior to those of bone tissue due to their reliance on reversible covalent bonds or other physical crosslinking methods. Critical-sized bone defect require a scaffold with sufficient strength to support new tissue formation [43]. Our hydrogel encapsulating a dual-sided centripetal microgrooved PLCL disk not only enhanced mechanical strength but also regulated cell migration, promoting bone regeneration.

Next, we examined the behavior of hydrogels in a PBS environment. As shown in Fig. S5, the freeze-dried hydrogels underwent rapid expansion within 2 h, achieving swelling equilibrium after 3 h, indicating their capacity to absorb and retain water. Additionally, during hydrogels degradation, the release of PB and PB@PLS nanoparticles were controlled (Fig. 3o). The release profiles indicated that PB nanoparticles effectively transported PLS without compromising the integrity of the 3D network structures.

3.3. Antioxidant properties of the PB@PLS co-cultured with BMSCs *in vitro*

Elevated intracellular ROS levels damage osteoblasts and induce apoptosis. ROS-scavenging biomaterials mitigate oxidative stress, promoting bone regeneration. Osteo-immunomodulatory biomaterials further enhance repair by balancing immune response and bone metabolism [44]. To evaluate the ROS-scavenging activity of PB@PLS, H₂O₂ was applied to stimulate BMSCs [20]. Firstly, the concentrations of BMSCs sensitive to H₂O₂ and PB@PLS were explored respectively

(Figs. S6a and b). 750 μ M H₂O₂ and 20 μ g/mL PB@PLS were finally selected for subsequent experiments. After 12 h of continuous stimulation, BMSCs exposed to H₂O₂ exhibited significantly elevated ROS levels, as indicated by strong red fluorescence (Fig. 4a). The introduction of PB and PB@PLS notably reduced the fluorescence signal, with PB@PLS demonstrating the most substantial decrease (Fig. 4b). Quantitative analysis using the CCK-8 assay further confirmed that PB effectively mitigated ROS and rescued the cells from H₂O₂-induced damage (Fig. 4c). Importantly, the combination of PLS and PB yielded a higher clearance rate compared to PB used alone. Immunomodulators balance inflammatory responses and mitigate drug-resistant bacterial infections. Reducing intracellular ROS in implantable scaffolds further minimizes infection risk [45,46].

3.4. Evaluation of the behavior of BMSCs on PLCL films

The substrate structure interfacing with the cells is strategically engineered to positively modulate their arrangement and behavior, thereby regulating their spreading morphology and guiding their migration direction. This approach can effectively enhance the recruitment of repair cells to the defect site [47,48]. To investigate the arrangement of BMSCs on the MG-PLCL/pep film, we performed fluorescent staining of actin filaments and nuclei [49]. As shown in Fig. S7, the fluorescence on F-PLCL film exhibited a cloud-like distribution, whereas MG-PLCL film displayed a centripetal stripe pattern. Although the centripetal radial grooves of MG-PLCL/pep film were stained, the cellular structure was not discernible due to the adsorption of dye. Under high magnification, the cytoskeleton in cells on F-PLCL film appeared randomly arranged with irregular spreading (Fig. 5a). In contrast, the majority of cells on MG-PLCL film and MG-PLCL/pep film were primarily located within the microgrooves, with the remaining cells situated on the ridges. These cells were noticeably elongated and oriented along the centripetal microgrooves. Despite significant

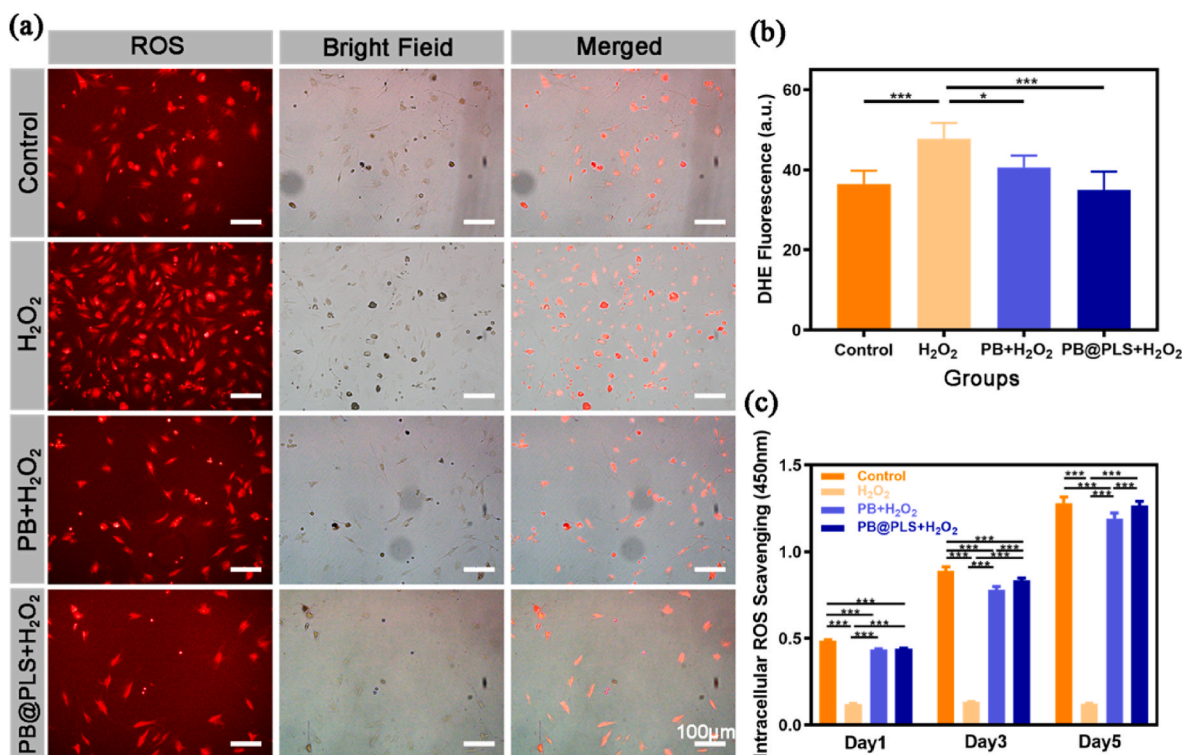


Fig. 4. Antioxidant properties of the PB@PLS co-cultured with BMSCs *in vitro*. (a) Representative fluorescence images of BMSCs stained with DHE after 12 h incubation with 750 μ M H₂O₂ and 20 μ g/mL concentrations of PB or PB@PLS nanoparticles. (b) Fluorescence quantitative analysis based on the relative images. (c) The intracellular ROS scavenging of PB and PB@PLS for 1, 3 and 5 days by CCK-8 assay. H₂O₂ concentrations: 750 μ M, PB or PB@PLS concentrations: 20 μ g/mL. All data are presented as mean \pm SD. One-way ANOVA for statistical analysis. * p < 0.05, ** p < 0.01, *** p < 0.001.

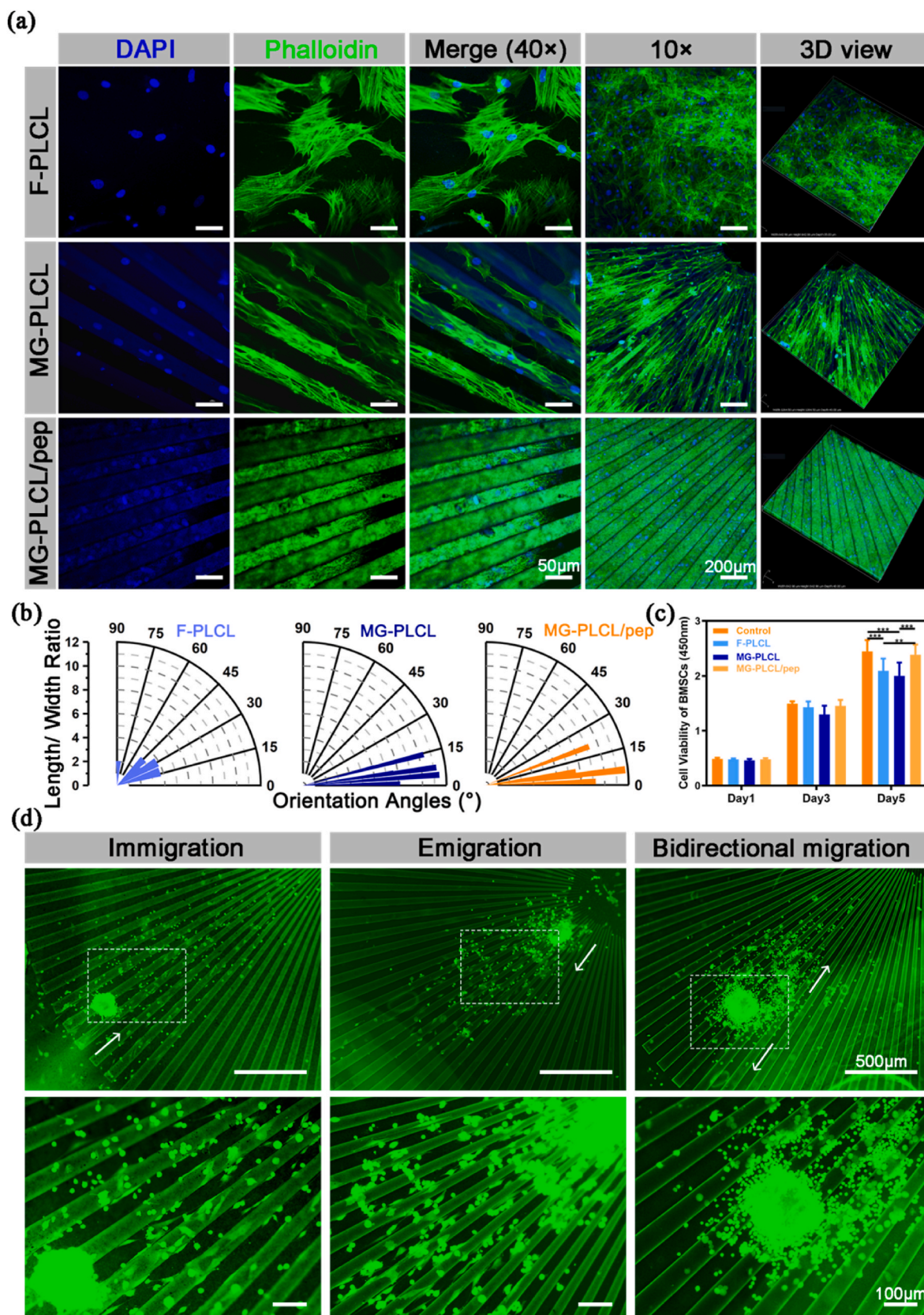


Fig. 5. Evaluation of the behavior of BMSCs on PLCL films. (a) Representative confocal images of BMSCs on various PLCL films. FITC-conjugated phalloidin staining of cell F-actin filaments is shown in green, and DAPI-stained cell nuclei are shown in blue. (b) Length/width ratio and orientation angles of BMSCs on various surfaces calculated by confocal images. The radius represents length/width ratio. The central angle represents the angle between the cell with the microgrooves. (c) Cell proliferation of BMSCs on various surfaces measured by CCK-8 assay. (d) The migration behavior of BMSCs spheroids on different positions of MG-PLCL/pep films. The white arrows indicate the migration direction of the spheroids. All data are presented as mean \pm SD. One-way ANOVA for statistical analysis. * $p < 0.05$, ** $p < 0.01$, *** $p < 0.001$.

non-specific adsorption on MG-PLCL/pep film, the F-actin filaments of the cells were aligned parallel to the direction of the grooves. We calculated the ratio of cell length to width on the surface, as well as the angle between the cell axis and the position of the groove (Fig. 5b). The length/width ratio of cells on F-PLCL film is 2.9 ± 0.68 , indicated that the cells spread evenly in all directions. In contrast, the ratios for MG-PLCL film and MG-PLCL/pep film were 9.2 ± 2.0 and 9.3 ± 2.1 , respectively. The increase in these ratios suggested that the micro-grooved architecture promoted cell extension, with no significant difference observed between the two groups (Fig. S8a). The orientation angles of F-PLCL film ranged from 13.0° to 88.0° , suggesting a random distribution of cells. In comparison, MG-PLCL film and MG-PLCL/pep film exhibited narrower distribution ranges of orientation angles, spanning from 1.2° to 14.8° and 1.8° – 20.4° , respectively (Fig. S8b). This indicated that the cells are predominantly arranged parallel to the microgrooves, which facilitates a more directed orientation distribution. In addition, the OD value of cells on MG-PLCL/pep film was significantly higher than that on PLCL film without pep after 5 days culture (Fig. 5c). The modification of pep markedly enhanced the adhesion of BMSCs onto the surfaces, which aligns with the nuclear fluorescence area observed in Fig. 5a. The substrate's architecture is designed to positively influence cell arrangement and behavior, controlling cell spreading and directing cell migration [47,48]. Cellular responses and activities are likely influenced by the ECM [6]. Substrate stiffness significantly affects cell adhesion, with cells generally adhering better to stiffer surfaces. Conversely, smooth surfaces can impede cell attachment [50,51]. Cells tend to spread more extensively on rigid 2D surfaces and also in softer 3D environments [41,52]. Our study demonstrated that cells tended to spread in microgrooved surfaces due to the cell-substrate interactions.

During bone regeneration, a significant number of cells accumulate at the injury site. We prepared BMSCs spheroids to mimic the natural status of aggregated cells and inoculated them at various locations on

the films to investigate the cell migration (Fig. 5d). Centrosymmetric films exhibit isotropic properties, therefore BMSC spheroids were inoculated at the edge, inner center, and middle of microgrooves to simulate cellular behavior in various positions during practical application. After 3 days of migration, cells at the edges primarily moved inward, while a significant number of cells located at the interior center tended to migrate outward. Notably, cells positioned in the middle exhibited greater inward migration, indicating a preference for moving toward narrower grooves. We hypothesized that variations in groove and ridge widths may differentially influence the migration of BMSCs. Within narrow grooves, BMSCs are more likely to reach both sides of the trench wall, thereby increasing the available sites for cell attachment. This suggested that the design of centripetal microgrooves is effective in promoting the migration of BMSCs toward areas of reduced width, thereby accelerating the repair process in central regions of bone defects. This was demonstrated by higher expression of osteogenesis related genes (*Col-1*, *ALP*, *Runx2*, *BSP*) on MG-PLCL film than that on F-PLCL film (Fig. S9 a). The microgrooved structure significantly regulates the cytoskeleton of cells, potentially influencing intracellular gene expression and osteogenic outcomes through epigenetic mechanisms. Additionally, co-culturing the entire scaffold with BMSCs demonstrated that the copper ions and peptides promoted the expression of key factors and proteins essential for bone regeneration (Fig. S9 b, c).

3.5. Evaluation of the behavior of various cells on PLCL films

The process of bone healing is complex and involves multiple cell types. The injured areas are populated not only by skeletal progenitor cells, stem cells, osteoblasts, and chondrocytes but also include various inflammatory, endothelial, hematopoietic, and other tissue cells [23]. Therefore, we further investigated the alignment and motility behavior of BMDMs, SCs and HUVECs [53].

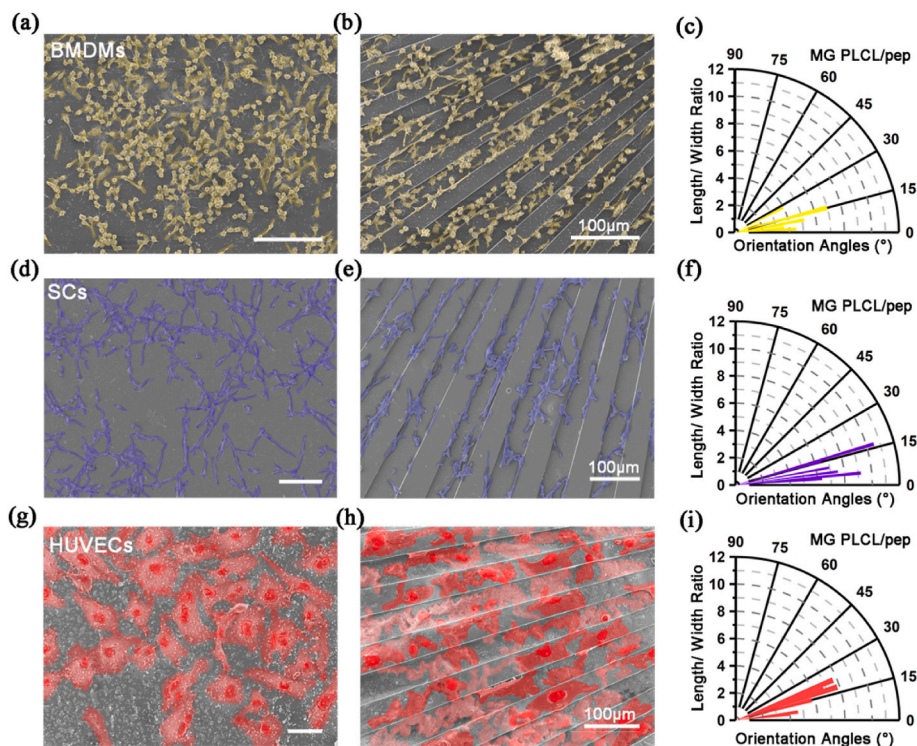


Fig. 6. Evaluation of the behavior of various cells on PLCL films. (a) Representative SEM images of BMDMs on F-PLCL/pep films. (b) SEM images of BMDMs on MG-PLCL/pep films. (c) Length/width ratio and orientation angles of BMDMs on MG-PLCL/pep films by SEM. The radius represents length/width ratio. The central angle represents the angle between the cells with the microgrooves. (d) SEM images of SCs on F-PLCL/pep films. (e) SEM images of SCs on MG-PLCL/pep films. (f) Length/width ratio and orientation angles of SCs on MG-PLCL/pep films by SEM. (g) SEM images of HUVECs on F-PLCL/pep films. (h) SEM images of HUVECs on MG-PLCL/pep films. (i) Length/width ratio and orientation angles of HUVECs on MG-PLCL/pep films calculated by SEM images. All data are presented as mean \pm SD.

BMDMs were extensively exposed on MG-PLCL/pep film (Fig. 6a and b). The cellular arrangement in the microgrooves was elongated due to topographical regulation, resulting in fewer branches compared to that observed on flat surfaces. The cells spread along the microgrooves in a spindle-like shape (Fig. S10 a). The orientation angles of spindle cells in grooves were nearly less than 45.0° (Fig. 6c). The cells length/width ratio of microgrooves was 3.8 ± 1.1 , whereas that of the flat BMDMs was 1.8 ± 0.5 . Macrophages exhibit distinct morphologies depending on their differentiation *in vitro* [54,55]. M1 macrophages display a fried-egg-like shape with extensions in all directions, while M2 macrophages become elongated and adopt a spindle shape (Fig. S10 b) [56]. We quantified the number of M1 and M2 macrophages in the same field of view based on their morphology (Fig. S10 c) and observed a significant increase in the proportion of M2 macrophages on the MG-PLCL film, suggesting that microgrooves promote macrophages differentiation towards the anti-inflammatory M2 phenotype [13]. Additionally, we performed immunofluorescence staining for M1 and M2 polarization markers in RAW264.7 cells, using CCR7 as a membrane marker for M1 macrophages and CD206 for M2 macrophages (Fig. S10 d). Comparison between the F-PLCL and MG-PLCL groups revealed no significant difference in CCR7 expression. However, the MG-PLCL film facilitated the differentiation of macrophages towards the M2 phenotype, resulting in high CD206 expression. Consequently, quantitative analysis indicated an increased M2/M1 macrophage ratio, consistent with previous research findings in Fig. S10 c (Fig. S10 e).

In addition, we investigated SCs, the primary cells in peripheral nerves. Due to their characteristic fusiform shape, SCs provide a more intuitive means of monitoring cellular morphology compared to other species (Fig. 6d and e). Our findings indicated no significant differences in the length-to-width ratio between flat and microgroove substrates after three days of culture. However, a remarkable difference was observed in the orientation angles (Fig. 6f, Fig. S10 f). SCs on flat substrates exhibited orientation angles ranging from 1.1° to 88.9° , while those on microgrooves ranged from 1.2° to 48.4° . These results suggest that SCs preferentially align along the microgrooves, whereas cells on flat surfaces exhibit random growth patterns. Additionally, CCK-8 assays confirmed that SCs can effectively proliferate on MG-PLCL/pep films (Fig. S10 g).

We investigated the gene expression of HUVECs associated with angiogenesis on scaffolds. SEM images revealed that the long axis of the HUVEC nuclei aligned nearly parallel to the grooves of the film (Fig. 6g, h, i). Additionally, the cells demonstrated proliferation on the film (Fig. S10 h). Our findings indicated that the incorporation of microgrooves and peptides enhances the expression levels of vasostimulating genes, such as *VEcad*, *PDGF β* , *CD31*, *VEGF α* , *HIF1*, and *Ang1*. This enhancement was likely a key factor in the ability of MG-PLCL/pep films to synergistically promote bone regeneration (Fig. S11).

3.6. Bone regeneration assessment *in vivo*

Before the evaluation *in vivo*, we first verified the biocompatibility of the scaffold extract *in vitro* (Fig. S12 a). The results confirmed that motivated by the promising performance of scaffolds osteoinductivity, angiogenesis, the regulation of redox homeostasis and migration *in vitro*.

Bone repair scaffolds inevitably come into direct or indirect contact with blood *in vivo* [57]. The scaffolds' hemocompatibility was assessed via co-culture with blood cells [58]. A hemolysis assay showed no hemolysis after 12 h of contact between the scaffolds and red blood cells, unlike the Triton X-100 positive control which exhibited significant hemolysis (Fig. S12b). Quantitative analysis showed no significant absorbance difference between the scaffold groups and the PBS control, confirming good hemocompatibility (Fig. S12c). To assess thrombosis risk, blood coagulation index (BCI) and blood recalcification time were measured (Fig. S12d). After adding a procoagulant agent, clotting time fell within the normal range (Fig. S12e), indicating good

biocompatibility comparable to PBS.

Hence, we further evaluated its potential as a substitute for bone regeneration *in vivo* in rat model with a large calvarial defect (Fig. 7a and b). The rats without intervention as control group compared with groups treated scaffolds owned different components (Table 1). After 8 weeks of transplanted the scaffold in rats, H&E staining of major organs, including the heart, liver, spleen, lung, and kidney, were not significantly different between groups (Fig. S13). Hence, the scaffolds were biocompatible in animals and had potential for *in vivo* application. 3D micro-CT imaging revealed significant bone regeneration in group D, demonstrating effective repair. This was followed by Group C, Group B and Group A (Fig. 7c). There was almost no bone formation in the Control group because of the difficult repair capacity. In addition, the micro-CT data was quantitatively analyzed. The bone mineral density (BMD) of Control, A, B, C and D groups were $0.25 \pm 0.01 \text{ g cm}^{-3}$, $0.29 \pm 0.01 \text{ g cm}^{-3}$, $0.33 \pm 0.01 \text{ g cm}^{-3}$, $0.35 \pm 0.03 \text{ g cm}^{-3}$ and $0.39 \pm 0.03 \text{ g cm}^{-3}$, respectively (Fig. 7d). The bone volume/total volumes (BV/TV) were $6.46 \pm 2.89 \%$, $11.44 \pm 3.63 \%$, $15.78 \pm 1.82 \%$, $18.68 \pm 1.75 \%$ and $22.33 \pm 1.98 \%$ (Fig. 7e). The BMD and BV/TV values of the treatment groups receiving macropatterned PLCL films (B, C, D group) were significantly higher than those without films, which means the performance of promoting bone regeneration were better. Histological examination used H&E staining and Masson's trichrome staining supported the results of micro-CT, confirming an enhanced therapeutic effect with significant fibrosis and new bone formation in group D (Fig. S14).

4. Conclusion

Inspired by the architecture of spider webs, we have developed a novel artificial scaffold that integrates physical guidance with immune regulation for the repair of critical-sized bone defects. This scaffold consists of dual-sided centripetal microgrooved PLCL film combined with a dynamic hydrogel containing PB@PLS nanoparticles. The regular grooves and ridges on the PLCL film become wider as they approach the edge, with the width at the edge measuring $80 \mu\text{m}$. The morphology of the microgrooves remained intact after aminolysis, glutaraldehyde coupling and peptide grafting, demonstrating excellent stability. Compared to a flat surface, the microgrooves regulated cell alignment with a smaller orientation angle and induce cell migration from the periphery toward the center region. Moreover, the ROS level in BMSCs was significantly decreased when co-cultured with the PB@PLS nanoparticles. *In vivo* assessment indicated that the scaffold significantly enhanced new bone formation, as evidenced by an increased BV/TV ratio of $22.33 \pm 1.98 \%$ compared to the other groups. This study highlights the potential of scaffolds that integrate physical guidance and antioxidant properties for bone regeneration and other tissue engineering applications.

CRedit authorship contribution statement

You Wu: Writing – original draft, Methodology, Investigation, Formal analysis, Data curation. **Xiaokun Yue:** Methodology, Investigation, Formal analysis, Data curation. **Ying Zhang:** Methodology, Investigation. **Ning Yu:** Methodology, Formal analysis, Data curation. **Chengyan Ge:** Methodology, Investigation, Data curation. **Rui Liu:** Resources, Methodology, Investigation. **Zhongying Duan:** Resources, Investigation, Data curation. **Lilong Gao:** Supervision, Methodology. **Xinlong Zang:** Supervision, Investigation. **Xin Sun:** Writing – review & editing, Supervision, Project administration, Funding acquisition, Conceptualization. **Deteng Zhang:** Writing – review & editing, Supervision, Project administration, Investigation, Funding acquisition, Data curation, Conceptualization.

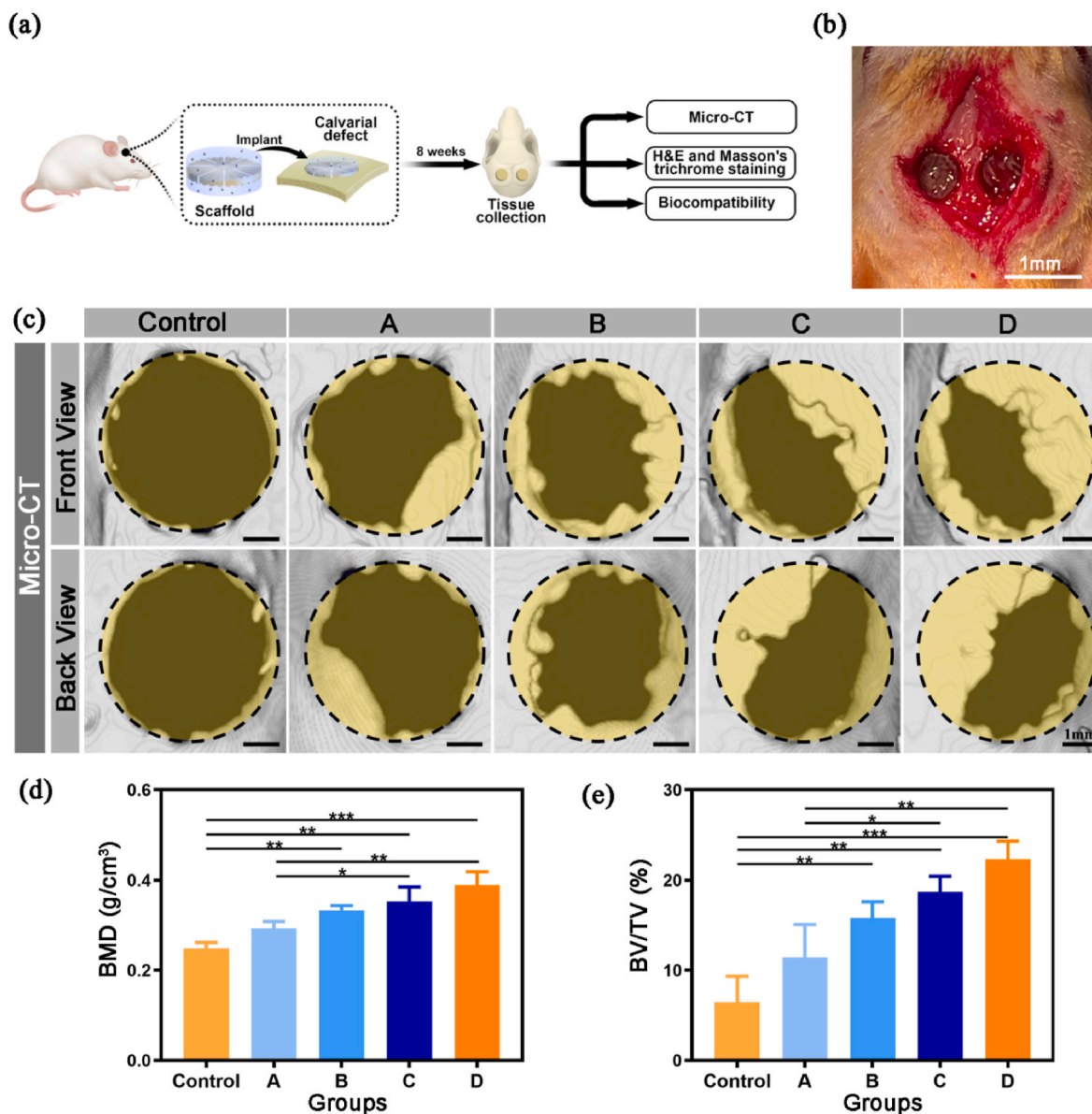


Fig. 7. Bone regeneration assessment *in vivo*. (a) Schematic illustrations of the application in critical-size bone defects repair of centripetal microgrooved scaffold. (b) Typical photograph of the established critical-size bone defect model. (c) Micro-CT reconstruction results presenting the new bone area of different experimental groups. (d) Quantitative analysis of BMD after 8-week post-operation. (e) Quantitative analysis of BV/TV after 8-week post-operation. All data are presented as mean \pm SD. One-way ANOVA for statistical analysis. * $p < 0.05$, ** $p < 0.01$, *** $p < 0.001$.

Declaration of competing interest

The authors declare that they have no known competing financial interests or personal relationships that could have appeared to influence the work reported in this paper.

Acknowledgments

This work was supported by the National Natural Science Foundation of China (grant No. 82101457 and grant No. 82302676), the Shandong Provincial Natural Science Foundation of China (ZR2021QH218), and "Intergovernmental International Cooperation on Science and Technology Innovation" Key Special Project of China (No. 2024YFE0104100).

Appendix A. Supplementary data

Supplementary data to this article can be found online at <https://doi.org/10.1016/j.mtbio.2024.101436>.

[org/10.1016/j.mtbio.2024.101436](https://doi.org/10.1016/j.mtbio.2024.101436).

Data availability

Data will be made available on request.

References

- [1] S. Chen, H. Wang, V.L. Mainardi, G. Talo, A. McCarthy, J.V. John, M.J. Teusink, L. Hong, J. Xie, Biomaterials with structural hierarchy and controlled 3D nanotopography guide endogenous bone regeneration, *Sci. Adv.* 7 (31) (2021).
- [2] M.U.A. Khan, S.I.A. Razak, S. Rehman, A. Hasan, S. Qureshi, G.M. Stojanovic, Bioactive scaffold (sodium alginate)-g-(nHAp@SiO₂)@GO for bone tissue engineering, *Int. J. Biol. Macromol.* 222 (Pt A) (2022) 462–472.
- [3] G. Zhu, T. Zhang, M. Chen, K. Yao, X. Huang, B. Zhang, Y. Li, J. Liu, Y. Wang, Z. Zhao, Bone physiological microenvironment and healing mechanism: basis for future bone-tissue engineering scaffolds, *Bioact. Mater.* 6 (11) (2021) 4110–4140.
- [4] C.H. Mac, H.Y. Chan, Y.H. Lin, A.K. Sharma, H.L. Song, Y.S. Chan, K.J. Lin, Y.J. Lin, H.W. Sung, Engineering a biomimetic bone scaffold that can regulate redox homeostasis and promote osteogenesis to repair large bone defects, *Biomaterials* 286 (2022) 121574.

- [5] M.U.A. Khan, S.I.A. Razak, M.N.M. Ansari, R.M. Zulkifli, N. Ahmad Zawawi, M. Arshad, Development of biodegradable bio-based composite for bone tissue engineering: synthesis, characterization and in vitro biocompatible evaluation, *Polymers* 13 (21) (2021).
- [6] M.U. Aslam Khan, H. Mehboob, S.I. Abd Razak, M.Y. Yahya, A.H. Mohd Yusof, M. H. Ramlie, T.J. Sahaya Anand, R. Hassan, A. Aziz, R. Amin, Development of polymeric nanocomposite (Xyloglucan-co-Methacrylic acid/hydroxyapatite/SiO₂) scaffold for bone tissue engineering applications-in-vitro antibacterial, cytotoxicity and cell culture evaluation, *Polymers* 12 (6) (2020).
- [7] X. Sun, X. Jiao, X. Yang, J. Ma, T. Wang, W. Jin, W. Li, H. Yang, Y. Mao, Y. Gan, X. Zhou, T. Li, S. Li, X. Chen, J. Wang, 3D bioprinting of osteon-mimetic scaffolds with hierarchical microchannels for vascularized bone tissue regeneration, *Biofabrication* 14 (3) (2022).
- [8] X. Zhang, Y. Xia, J. Xu, J. Kang, X. Li, Y. Li, W. Yan, F. Tian, B. Zhao, B. Li, C. Wang, L. Wang, Cell-free chitosan/silk fibroin/bioactive glass scaffolds with radial pore for in situ inductive regeneration of critical-size bone defects, *Carbohydr. Polym.* 332 (2024) 121945.
- [9] E. Bosch-Rue, L. Diez-Tercero, J.O. Buitrago, E. Castro, R.A. Perez, Angiogenic and immunomodulation role of ions for initial stages of bone tissue regeneration, *Acta Biomater.* 166 (2023) 14–41.
- [10] Z. Min, Z. Shichang, X. Chen, Z. Yufang, Z. Changqing, 3D-printed dimethylallyl glycine delivery scaffolds to improve angiogenesis and osteogenesis, *Biomater. Sci.* 3 (8) (2015) 1236–1244.
- [11] D. Zhang, S. Xu, S. Wu, C. Gao, Micropatterned poly(d,l-lactide-co-caprolactone) films entrapped with gelatin for promoting the alignment and directional migration of Schwann cells, *J. Mater. Chem. B* 6 (8) (2018) 1226–1237.
- [12] D. Zhang, S. Wu, J. Feng, Y. Duan, D. Xing, C. Gao, Micropatterned biodegradable polyesters clicked with CQAASIKVAV promote cell alignment, directional migration, and neurite outgrowth, *Acta Biomater.* 74 (2018) 143–155.
- [13] X. Dong, S. Liu, Y. Yang, S. Gao, W. Li, J. Cao, Y. Wan, Z. Huang, G. Fan, Q. Chen, H. Wang, M. Zhu, D. Kong, Aligned microfibril-induced macrophage polarization to guide schwann-cell-enabled peripheral nerve regeneration, *Biomaterials* 272 (2021) 120767.
- [14] B. Jin, Y. Yu, C. Lou, X. Zhang, B. Gong, J. Chen, X. Chen, Z. Zhou, L. Zhang, J. Xiao, J. Xue, Combining a density gradient of biomacromolecular nanoparticles with biological effectors in an electrospun fiber-based nerve guidance conduit to promote peripheral nerve repair, *Adv. Sci.* 10 (4) (2023) e2203296.
- [15] S. Chen, A. McCarthy, J.V. John, Y. Su, J. Xie, Converting 2D nanofiber membranes to 3D hierarchical assemblies with structural and compositional gradients regulates cell behavior, *Adv. Mater.* 32 (43) (2020) e2003754.
- [16] D. Zhang, Z. Li, H. Shi, Y. Yao, W. Du, P. Lu, K. Liang, L. Hong, C. Gao, Micropatterns and peptide gradient on the inner surface of a guidance conduit synergistically promotes nerve regeneration in vivo, *Bioact. Mater.* 9 (2022) 134–146.
- [17] T. Mulder, L. Wilkins, B. Mortimer, F. Vollrath, Dynamic environments do not appear to constrain spider web building behaviour, *Naturwissenschaften* 108 (3) (2021) 20.
- [18] I. Su, N. Narayanan, M.A. Logrono, K. Guo, A. Bisshop, R. Muhlethaler, T. Saraceno, M.J. Buehler, In situ three-dimensional spider web construction and mechanics, *Proc. Natl. Acad. Sci. U. S. A.* 118 (33) (2021).
- [19] X. Zheng, X. Pan, Q. Pang, C. Shuai, L. Ma, C. Gao, Selective capture of mesenchymal stem cells over fibroblasts and immune cells on E7-modified collagen substrates under flow circumstances, *J. Mater. Chem. B* 6 (1) (2018) 165–173.
- [20] H. Wang, F. Lin, Y. Wu, W. Guo, X. Chen, C. Xiao, M. Chen, Carrier-free nanodrug based on Co-assembly of methylprednisolone dimer and rutin for combined treatment of spinal cord injury, *ACS Nano* 17 (13) (2023) 12176–12187.
- [21] Q. Guo, T. Yin, W. Huang, R. Nan, T. Xiang, S. Zhou, Hybrid hydrogels for immunoregulation and proangiogenesis through mild heat stimulation to accelerate whole-process diabetic wound healing, *Adv. Healthcare Mater.* 13 (18) (2024) e2304536.
- [22] D. Zhang, J. Song, Z. Jing, H. Qin, Y. Wu, J. Zhou, X. Zang, Stimulus responsive nanocarrier for enhanced antitumor responses against hepatocellular carcinoma, *Int. J. Nanomed.* 19 (2024) 13339–13355.
- [23] A. Ho-Shui-Ling, J. Bolander, L.E. Rustom, A.W. Johnson, F.P. Luyten, C. Picart, Bone regeneration strategies: engineered scaffolds, bioactive molecules and stem cells current stage and future perspectives, *Biomaterials* 180 (2018) 143–162.
- [24] X. Farto-Vaamonde, G. Auriemma, R.P. Aquino, A. Concheiro, C. Alvarez-Lorenzo, Post-manufacture loading of filaments and 3D printed PLA scaffolds with prednisolone and dexamethasone for tissue regeneration applications, *Eur. J. Pharm. Biopharm.* 141 (2019) 100–110.
- [25] F. Mohammadi, N. Tanideh, S. Mohammadi Samani, F. Ahmadi, Efficacy of a hybrid system of hyaluronic acid and collagen loaded with prednisolone and TGF- β 3 for cartilage regeneration in rats, *J. Drug Deliv. Sci. Technol.* 51 (2019) 55–62.
- [26] A. Mohamed, V. Korzhikov-Vlakh, N. Zhang, A. Said, I. Pilipenko, M. Schafer-Korting, C. Zoschke, T. Tennikova, Effect of poly(L-lysine) and heparin coatings on the surface of polyester-based particles on prednisolone release and biocompatibility, *Pharmaceutics* 13 (6) (2021).
- [27] K. Zhang, M. Tu, W. Gao, X. Cai, F. Song, Z. Chen, Q. Zhang, J. Wang, C. Jin, J. Shi, X. Yang, Y. Zhu, W. Gu, B. Hu, Y. Zheng, H. Zhang, M. Tian, Hollow Prussian blue nanozymes drive neuroprotection against ischemic stroke via attenuating oxidative stress, counteracting inflammation, and suppressing cell apoptosis, *Nano Lett.* 19 (5) (2019) 2812–2823.
- [28] H. He, M. Long, Y. Duan, N. Gu, Prussian blue nanozymes: progress, challenges, and opportunities, *Nanoscale* 15 (31) (2023) 12818–12839.
- [29] C. Cho, H. Oh, J.S. Lee, L.J. Kang, E.J. Oh, Y. Hwang, S.J. Kim, Y.S. Bae, E.J. Kim, H.C. Kang, W.I. Choi, S. Yang, Prussian blue nanozymes coated with Pluronic attenuate inflammatory osteoarthritis by blocking c-Jun N-terminal kinase phosphorylation, *Biomaterials* 297 (2023) 122131.
- [30] X. Xue, Y. Hu, S. Wang, X. Chen, Y. Jiang, J. Su, Fabrication of physical and chemical crosslinked hydrogels for bone tissue engineering, *Bioact. Mater.* 12 (2022) 327–339.
- [31] R. Yang, G. Li, C. Zhuang, P. Yu, T. Ye, Y. Zhang, P. Shang, J. Huang, M. Cai, L. Wang, W. Cui, L. Deng, Gradient bimetallic ion-based hydrogels for tissue microstructure reconstruction of tendon-to-bone insertion, *Sci. Adv.* 7 (26) (2021).
- [32] X. Sun, J. Yang, J. Ma, T. Wang, X. Zhao, D. Zhu, W. Jin, K. Zhang, X. Sun, Y. Shen, N. Xie, F. Yang, X. Shang, S. Li, X. Zhou, C. He, D. Zhang, J. Wang, Three-dimensional bioprinted BMSCs-laden highly adhesive artificial periosteum containing gelatin-dopamine and graphene oxide nanosheets promoting bone defect repair, *Biofabrication* 15 (2) (2023).
- [33] Y.J. Ha, X.J. Ma, S.K. Li, T. Li, Z.H. Li, Y.H. Qian, M. Shafiq, J.W. Wang, X.J. Zhou, C.L. He, Bone microenvironment-mimetic scaffolds with hierarchical microstructure for enhanced vascularization and bone regeneration, *Adv. Funct. Mater.* 32 (20) (2022).
- [34] D. Zhang, Y. Yao, Y. Duan, X. Yu, H. Shi, J.R. Nakkala, X. Zuo, L. Hong, Z. Mao, C. Gao, Surface-anchored graphene oxide nanosheets on cell-scale micropatterned poly(d,l-lactide-co-caprolactone) conduits promote peripheral nerve regeneration, *ACS Appl. Mater. Interfaces* 12 (7) (2020) 7915–7930.
- [35] X. Sun, Z. Ma, X. Zhao, W. Jin, C. Zhang, J. Ma, L. Qiang, W. Wang, Q. Deng, H. Yang, J. Zhao, Q. Liang, X. Zhou, T. Li, J. Wang, Three-dimensional bioprinting of multicell-laden scaffolds containing bone morphogenic protein-4 for promoting M2 macrophage polarization and accelerating bone defect repair in diabetes mellitus, *Bioact. Mater.* 6 (3) (2021) 757–769.
- [36] L. Xiao, M. Wu, F. Yan, Y. Xie, Z. Liu, H. Huang, Z. Yang, S. Yao, L. Cai, A radial 3D polycaprolactone nanofiber scaffold modified by biomineralization and silk fibroin coating promote bone regeneration in vivo, *Int. J. Biol. Macromol.* 172 (2021) 19–29.
- [37] Y. Zhu, Z. Mao, C. Gao, Control over the gradient differentiation of rat BMSCs on a PCL membrane with surface-immobilized alendronate gradient, *Biomacromolecules* 14 (2) (2013) 342–349.
- [38] S. Yu, Z. Mao, C. Gao, Preparation of gelatin density gradient on poly(epsilon-caprolactone) membrane and its influence on adhesion and migration of endothelial cells, *J. Colloid Interface Sci.* 451 (2015) 177–183.
- [39] H. He, Q. Han, S. Wang, M. Long, M. Zhang, Y. Li, Y. Zhang, N. Gu, Design of a multifunctional nanozyme for resolving the proinflammatory plaque microenvironment and attenuating atherosclerosis, *ACS Nano* 17 (15) (2023) 14555–14571.
- [40] K.M. McAndrews, M.J. Kim, T.Y. Lam, D.J. McGrail, M.R. Dawson, Architectural and mechanical cues direct mesenchymal stem cell interactions with crosslinked gelatin scaffolds, *Tissue Eng. Part A* 20 (23–24) (2014) 3252–3260.
- [41] H. Cao, L. Duan, Y. Zhang, J. Cao, K. Zhang, Current hydrogel advances in physicochemical and biological response-driven biomedical application diversity, *Signal Transduct. Targeted Ther.* 6 (1) (2021) 426.
- [42] P. Wang, S. Yang, Y. Liu, Y. Zhao, C. Wang, Modified Bouc-Wen model based on a fractional derivative for describing the hysteretic characteristics of magnetorheological elastomers, *Chin. J. Eng.* 44 (3) (2022) 389–401.
- [43] L. Shanmuganatha, M.U.A. Khan, A. Sulong, M.L. Ramli, A. Baharudin, H. M. Ariffin, S.I.A. Razak, M.H. Ng, Characterization of titanium ceramic composite for bone implants applications, *Ceram. Int.* 48 (16) (2022) 22808–22819.
- [44] R. Wang, X. He, S. Su, J. Bai, Q. Xiang, H. Liu, F. Zhou, Advances in smart biomaterials that modulate the bone microenvironment to promote bone defect repair in diabetes mellitus, *Smart Mater. Med.* 5 (3) (2024) 359–372.
- [45] S. Zhang, H. Yang, M. Wang, D. Mantovani, K. Yang, F. Witte, L. Tan, B. Yue, X. Qu, Immunomodulatory biomaterials against bacterial infections: progress, challenges, and future perspectives, *Innovation* 4 (6) (2023) 100503.
- [46] X. Chen, X. Li, W. He, M. Wang, A. Gao, L. Tong, S. Guo, H. Wang, G. Pan, Rational multivalency construction enables bactericidal effect amplification and dynamic biomaterial design, *Innovation* 4 (5) (2023) 100483.
- [47] H. Pan, Y. Wei, C. Zeng, G. Yang, C. Dong, W. Wan, S. Chen, Hierarchically assembled nanofiber scaffold guides long bone regeneration by promoting osteogenic/chondrogenic differentiation of endogenous mesenchymal stem cells, *Small* 20 (26) (2024) e2309868.
- [48] R. Fan, J. Zhao, L. Yi, J. Yuan, A. McCarthy, B. Li, G. Yang, J.V. John, W. Wan, Y. Zhang, S. Chen, Anti-inflammatory peptide-conjugated silk fibroin/cryogel hybrid dual fiber scaffold with hierarchical structure promotes healing of chronic wounds, *Adv. Mater.* 36 (16) (2024) e2307328.
- [49] W. Oosterheert, B.U. Klink, A. Belys, S. Pospich, S. Raunser, Structural basis of actin filament assembly and aging, *Nature* 611 (7935) (2022) 374–379.
- [50] Y. Gu, Y. Ji, Y. Zhao, Y. Liu, F. Ding, X. Gu, Y. Yang, The influence of substrate stiffness on the behavior and functions of Schwann cells in culture, *Biomaterials* 33 (28) (2012) 6672–6681.
- [51] P.U. Shirke, H. Goswami, V. Kumar, D. Shah, S. Beri, S. Das, J. Bellare, S. Mayor, K. V. Venkatesh, J.R. Seth, A. Majumder, "Viscotaxis"-directed migration of mesenchymal stem cells in response to loss modulus gradient, *Acta Biomater.* 135 (2021) 356–367.
- [52] H. Cao, M.K.H. Lee, H. Yang, S.K. Sze, N.S. Tan, C.Y. Tay, Mechanoregulation of cancer-associated fibroblast phenotype in three-dimensional interpenetrating hydrogel networks, *Langmuir* 35 (23) (2019) 7487–7495.
- [53] T.C. Wang, W.T. Li, Y.X. Zhang, X. Xu, L. Qiang, W.Q. Miao, X.K. Yue, X. Jiao, X. H. Zhou, Z.J. Ma, S. Li, M.L. Ding, J.F. Zhu, C. Yang, H. Wang, T. Li, X. Sun, J. W. Wang, Bioprinted constructs that simulate nerve-bone crosstalk to improve microenvironment for bone repair, *Bioact. Mater.* 27 (2023) 377–393.

- [54] F.Y. McWhorter, T. Wang, P. Nguyen, T. Chung, W.F. Liu, Modulation of macrophage phenotype by cell shape, *Proc. Natl. Acad. Sci. U. S. A.* 110 (43) (2013) 17253–17258.
- [55] H. Cho, H.Y. Kwon, A. Sharma, S.H. Lee, X. Liu, N. Miyamoto, J.J. Kim, S.H. Im, N. Y. Kang, Y.T. Chang, Visualizing inflammation with an M1 macrophage selective probe via GLUT1 as the gating target, *Nat. Commun.* 13 (1) (2022) 5974.
- [56] R. Lou, J. Chen, F. Zhou, T. Zhang, X. Chen, C. Wang, B. Guo, L. Lin, Exosomal miRNA-155-5p from M1-polarized macrophages suppresses angiogenesis by targeting GDF6 to interrupt diabetic wound healing, *Mol. Ther. Nucleic Acids* 34 (2023) 102074.
- [57] M.U. Aslam Khan, A. Haider, S.I. Abd Razak, M.R. Abdul Kadir, S. Haider, S. A. Shah, A. Hasan, R. Khan, S.D. Khan, I. Shakir, Arabinoxylan/graphene-oxide/nHAp-NPs/PVA bionano composite scaffolds for fractured bone healing, *J. Tissue Eng. Regen. Med.* 15 (4) (2021) 322–335.
- [58] T. Xia, F. Xie, X. Bian, Z. Chen, S. Zhang, Z. Fang, Q. Ye, J. Cai, Y. Wang, Ultrabroad-spectrum, multidrug resistant bacteria-killing, and biocompatible quaternized chitin derivative for infected wound healing, *Mater. Sci. Eng. C Mater. Biol. Appl.* 126 (2021) 112177.